



<https://technobius.kz/>

e-ISSN  
3007-0147

# Technobius Physics

*A peer-reviewed open-access journal*

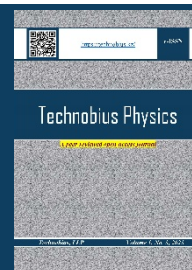
*Technobius, LLP*

*Volume 2, No. 1, 2024*



# Technobius Physics

Volume 2, No. 1, 2024



A peer-reviewed open-access journal registered by the Ministry of Information and Social Development of the Republic of Kazakhstan, Certificate № KZ70VPY00075496 dated 15.08.2023




**ISSN (Online):** 3007-0147

**Thematic Directions:** General Physics, Condensed Matter Physics


**Publisher:** Technobius, LLP

**Address:** 2 Turkestan street, office 116, 010000, Astana, Republic of Kazakhstan

















## Editor-in-Chief:

   *Aida Nazarova*, PhD, Laboratory Assistant, Department of Physics, Nazarbayev University, Astana, Kazakhstan

## Technical Editor:

   *Saeed Nasiri*, Dr, Professor, Department of Physics, Nazarbayev University, Astana, Kazakhstan

## Editors:

-   *Sang Ma Lee*, Dr., Professor, Engineering Research Center for Net Shape and Die Manufacturing, Pusan National University, Busan, South Korea
-   *Suk Bong Kang*, Dr., Professor, Korea Institute of Materials Science, Changwon, South Korea
-   *Marshall Onellion*, Dr., Professor, Department of Physics, University of Wisconsin-Madison, Madison, United States
-    *Bill Wheatle*, Dr, Assistant Professor, McKetta Department of Chemical Engineering, The University of Texas at Austin, Austin, United States
-   *Hyun-ho Kim*, Dr, Assistant Professor, School of Mechanical Engineering, Pusan National University, Busan, South Korea
-   *Yong-phil Jeon*, Dr., Precision Manufacturing System Division, Pusan National University, Busan, South Korea
-    *Marius Schwarz*, Dr., Assistant Professor, Department of Civil Engineering, University North, Varaždin, Croatia

**Copyright:** © Technobius, LLP

**Contacts:** Website: <https://technobius.kz/>  
E-mail: [technobiusphysics@gmail.com](mailto:technobiusphysics@gmail.com)

CONTENTS

Title and Authors	Category	No.
Comparative analysis of copper X-radiation intensity with LiF and KBr crystals <i>Dias Sagatov</i>	<i>Condensed Matter Physics</i>	0007
Design of magnetic field sensor with software for a wide range of applications <i>Ruslan Kalibek, Daria Sopyryaeva</i>	<i>General Physics</i>	0008
Harnessing ultrawideband technology for enhanced communication and radar detection <i>Adil Karimov</i>	<i>General Physics</i>	0009
Corrigendum to “D. Sagatov, “Comparative analysis of copper X-radiation intensity with LiF and KBr crystals”, tbusphys, vol. 2, no. 1, p. 0007, Jan. 2024. doi: 10.54355/tbusphys/2.1.2024.0007”	<i>Condensed Matter Physics</i>	0007c
Corrigendum to “A. Karimov, “Harnessing ultrawideband technology for enhanced communication and radar detection”, tbusphys, vol. 2, no. 1, p. 0009, Mar. 2025. doi: 10.54355/tbusphys/2.1.2024.0009”	<i>General Physics</i>	0009c



**Corrigendum Notice: A corrigendum has been issued for this article and is included at the end of this document.**

Article

## Comparative analysis of copper X-radiation intensity with LiF and KBr crystals

 Dias Sagatov\*

Laboratory of Energy Storage Systems, National Laboratory Astana, 53 Kabanbay ave., Astana, Kazakhstan

\*Correspondence: [dias.sagatov@list.ru](mailto:dias.sagatov@list.ru)

**Abstract.** The intensity of copper X-radiation has been scrutinized as a function of the Bragg angle, employing both LiF and KBr crystals. X-ray intensity spectra were recorded for Cu as a function of Bragg angle using LiF, KBr single crystals using a PHYWE X-Ray Expert Unit (35 kV, 1 mA) with an X-ray goniometer, Plug-in Cu X-ray tube and a 2.2 mm diameter aperture tube. The scanning range was chosen to be  $4^{\circ}$ - $55^{\circ}$  for LiF and  $3^{\circ}$ - $75^{\circ}$  for KBr. The resultant spectra furnish a comprehensive portrayal of the variation in X-ray emission intensity relative to alterations in the Bragg angle. This investigation contributes to our comprehension of crystallographic phenomena and underscores the efficacy of diverse crystalline materials in X-ray diffraction studies. Precise determinations of the energy levels for characteristic copper X-ray lines have been obtained, revealing  $E(K\beta) = 8868.374 \pm 30.474$  eV and  $(K\alpha) = 8026.349 \pm 31.634$  eV. These findings accentuate the significance of X-ray spectroscopy in delineating the elemental composition and structural attributes of materials, while also affirming the role of theoretical predictions in elucidating experimental observations.

**Keywords:** X-ray spectroscopy, Bragg angle, copper X-radiation, crystallographic phenomena, energy determination.

### 1. Introduction

Undoubtedly, X-ray diffraction stands as the cornerstone of solid-state physics and chemistry, representing the most pivotal and extensively utilized technique within these fields. X-ray generation stemming from collisions between protons or light ions and atoms stands as a pivotal area of investigation for understanding inner-shell ionization mechanisms. This subject has undergone extensive examination from experimental and theoretical standpoints over recent decades, yielding significant insights. Notably, extensive collections of experimental X-ray cross-section data have been assembled for K and L shells ionized by protons and helium ions, enabling meticulous comparisons with established theoretical models [1–5].

When high-energy electrons collide with the metallic anode within an X-ray tube, they generate X-rays characterized by a continuous energy spectrum. Embedded within this continuum are specific X-ray lines, known as characteristic X-ray lines, which remain independent of the anode voltage and are unique to the composition of the anode material. These lines originate from the ionization of an anode atom's K shell when struck by an electron. Subsequently, the resulting vacancy within the shell is filled by an electron transitioning from a higher energy level. The energy liberated during this de-excitation process manifests as an X-ray emission distinct to the anode atom.

X-ray spectroscopy serves as a pivotal tool in the realm of material characterization, offering unparalleled insights into the elemental composition and structural properties of diverse substances. The analysis of X-ray emission intensity as a function of the Bragg angle, facilitated by crystals such as LiF and KBr, constitutes a fundamental aspect of X-ray diffraction studies [6–8]. This investigation aims to elucidate the intricate relationship between Bragg angle variations and copper X-radiation intensity, thereby advancing our understanding of crystallographic phenomena. Additionally, precise determinations of energy levels for characteristic copper X-ray lines further underscore the utility of X-ray spectroscopy in unraveling the intricacies of material properties. By combining experimental

observations with theoretical predictions, this study endeavors to provide a comprehensive framework for interpreting X-ray diffraction data and exploring the structural characteristics of materials at the atomic level [9-10].

The aim of this article is to explore and elucidate the phenomenon of X-ray production resulting from collisions between protons or other light ions and atoms. By examining this process from both experimental and theoretical perspectives, the article seeks to enhance our understanding of inner-shell ionization mechanisms. Additionally, it aims to provide detailed comparisons between experimental X-ray cross-section data and existing theoretical models, thereby advancing the current understanding of X-ray generation in such collisions.

## 2. Methods

X-ray diffraction spectra were collected using mounted single crystals of lithium fluoride (LiF) and potassium bromide (KBr), both with crystallographic orientation (100). Each crystal had a thickness of 1 mm and a usable surface area of  $10 \times 12$  mm. The LiF crystals were polished, while the KBr crystals remained unpolished. Crystals were sourced from Crystal GmbH (Germany) and assumed to be free of impurities. The known lattice spacings were 201.4 pm for LiF and 329 pm for KBr.

Measurements were performed using the HUBER X-ray Diffraction System, configured with the Copper Anode X-ray Tube (40 kV, 1 mA); Primary Beam Collimator (2.2 mm aperture); High-Precision Goniometer (HUBER 420); Geiger-Müller Detector (15 mm window, Ludlum or equivalent). A schematic of the experimental setup is shown in Figure 1.

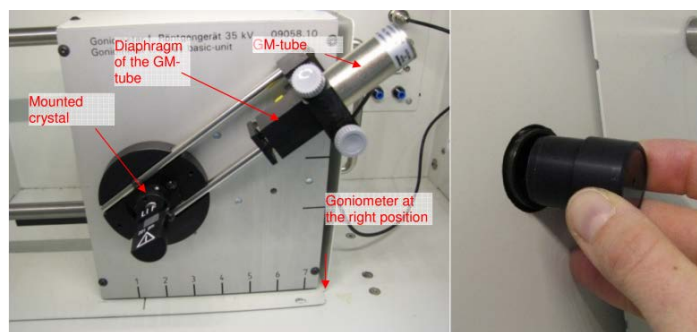


Figure 1 – Installation of X-ray goniometer and Geiger-Muller counter tube

The copper anode generated characteristic X-rays, which were directed onto the LiF or KBr crystal. The resulting diffracted beams were detected at various Bragg angles using the Geiger-Müller counter.

Intensity spectra were recorded as a function of the Bragg angle ( $\theta$ ) by rotating the goniometer-controlled crystal-detector stage. Scan parameters were for angular range:  $4^\circ$ – $55^\circ$  for LiF and  $3^\circ$ – $75^\circ$  for KBr; angle step width:  $0.1^\circ$ ; gate time: 2 s per point. All scanning procedures and data acquisition were performed using SPEC Control Software (Certified Scientific Software, USA). The goniometer system was calibrated using internal standards and factory-aligned optics. All experiments were carried out under ambient laboratory conditions without additional vacuum or environmental control.

The X-ray intensity spectra have been recorded for copper as a function of Bragg angle using mounted LiF, KBr single crystals. Crystals were sourced from Crystal GmbH (Germany) and assumed to be free of impurities. X-ray spectra were recorded using a PHYWE X-Ray Expert Unit (35 kV, 1mA) with X-ray goniometer, X-ray Plug-in Cu tube and Diaphragm tube with the diameter of 2.2 mm (Figure 1). An X-ray tube with a copper anode generates X-radiation that is selected with the aid of a mounted crystal (LiF and KBr) as a function of the Bragg angle. A Geiger-Muller counter tube with the size of 15 mm measures the intensity of the radiation. The glancing angles of the characteristic X-ray lines are then used to determine the energy. The spectra were scanned in the

range  $4^{\circ}$ - $55^{\circ}$  for LiF and  $3^{\circ}$ - $75^{\circ}$  for KBr with the gate time of 2 s and angle step width  $0.1^{\circ}$  using a XR 4.0 Software. The goniometer has been programmed for automatic calibration to obtain accurate reflection angles.

The Bragg angles ( $\theta$ ) obtained from the recorded intensity spectra were used to calculate the corresponding X-ray wavelengths ( $\lambda$ ) and photon energies ( $E$ ) using Bragg's law and the energy-wavelength relation:

$$\lambda = \frac{2d\sin\theta}{n} \text{ and } E = \frac{hc}{\lambda} \quad (1)$$

where  $d$  is the interplanar spacing,  $h$  is Planck's constant ( $6.626 \times 10^{-34}$  J·s),  $c$  is the speed of light ( $3.00 \times 10^8$  m/s), and  $n=1$  for first-order diffraction. Energies were expressed in electronvolts (eV).

To ensure reliability, each peak angle was measured in triplicate, and the mean and standard deviation (SD) of the measured angles were calculated. Propagation of error was applied to determine uncertainty in the calculated wavelengths and energies:

$$\sigma_E = \frac{dE}{d\theta} \cdot \sigma_{\theta} \quad (2)$$

$\sigma_{\theta}$  is the standard deviation of the angle measurements.

All statistical analyses, including mean, SD, and propagation of error, were performed using OriginPro 2020 (OriginLab Corporation, USA). Graphical representations of the spectra and energy distributions were also generated in OriginPro. Results were considered statistically reliable if relative uncertainties in peak energy were below 2%.

### 3. Results and Discussion

As is known, when high-energy electrons hit the metal anode of an X-ray tube, X-rays with a continuum energy distribution are produced. We have analyzed polychromatic X-rays using LiF and KBr crystals (Figure 2–3).

Figure 2 presents copper X-ray intensity spectra recorded in range of  $4^{\circ}$ - $55^{\circ}$  for LiF crystals. The curve has a distinct peaks overlaying the continuous spectrum of the bremsstrahlung. The positions of these peaks remain consistent regardless of fluctuations in the anode voltage, suggesting their characteristic nature as copper lines. The initial set of lines corresponds to the first order of diffraction ( $n = 1$ ), whereas the subsequent set corresponds to  $n = 2$ . This arises from the condition where X-rays of wavelength  $\lambda$  approach the crystal at an angle  $\nu$ , leading to constructive interference post-scattering only when the path difference  $\delta$  between the partial waves reflected from the lattice planes equals one or more wavelengths.

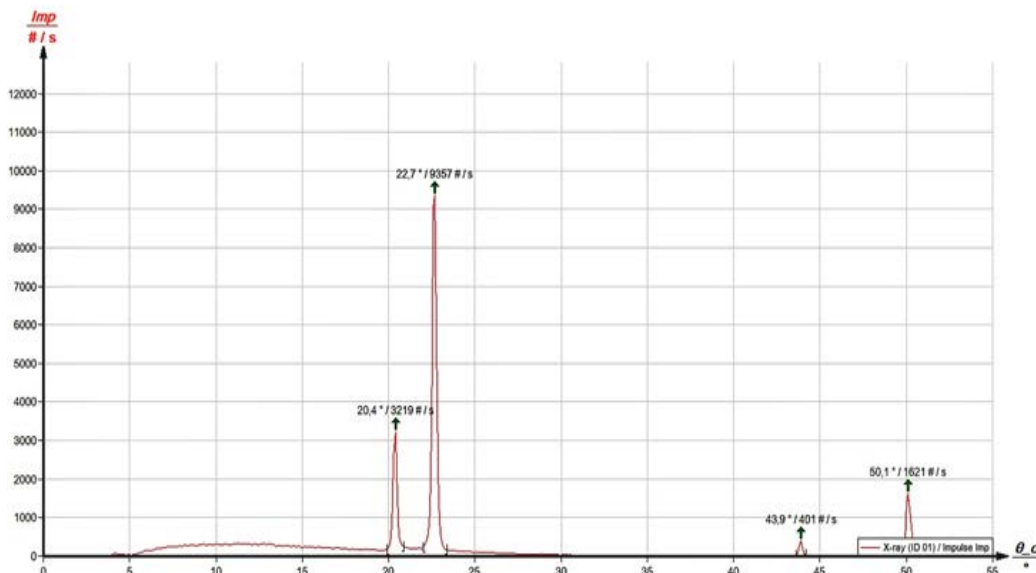


Figure 2 – Copper X-ray intensity as a function of the angle of incidence with LiF crystal as a Bragg analyzer



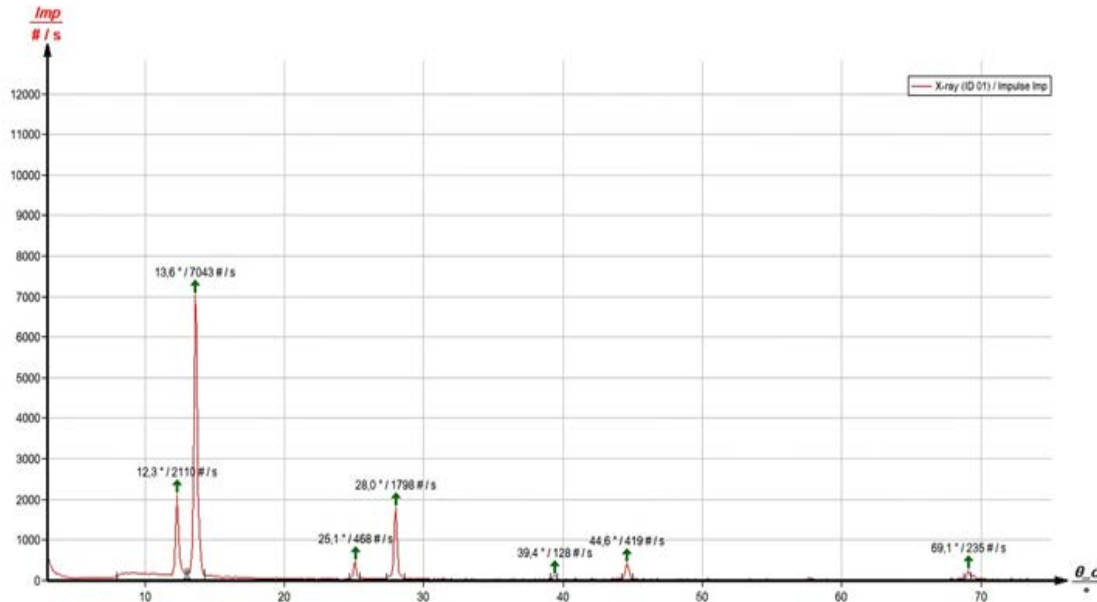


Figure 3 – Copper X-ray intensity as a function of the angle of incidence with KBr crystal as a Bragg analyzer

Substituting the LiF crystal with a KBr crystal in the examination of the copper X-ray spectrum permits Bragg scatterings up to the fourth order of diffraction ( $n = 4$ ) as illustrated in Figure 3. The supplementary patterns observed beyond those depicted in Figure 3 stem from the increased lattice constant of the KBr crystal. The maximums recorded during X-ray irradiation in range of  $3^\circ$ – $75^\circ$  also refer to characteristic copper peaks.

The bremsstrahlung spectrum depicted in Figure 3 exhibits a significant decrease in intensity towards smaller angles, notably at  $8.0^\circ$  and  $16.3^\circ$ . This decline aligns precisely with the theoretically anticipated bromide K absorption edge ( $E_K = 13.474$  keV) within the first and second orders of diffraction. However, the potassium, lithium, and fluorine K absorption edges remain undetectable due to the bremsstrahlung spectrum's insufficient intensity within these energy ranges.

The experimentally obtained values for the diffraction angles and their corresponding energies are summarized in Table 1 and Table 2.

Table 1 – Obtained experimental data of alkali halide crystals

Crystals	Initiation, deg	Maximum, deg	Shift, deg	Height, no/s	Area, no/s <sup>2</sup>
LiF	19.8	20.5	20.8	3220.0	1022.0
	22.1	22.8	23.2	9355.1	3123.4
	43.7	44.0	44.1	405.11	102.5
	49.7	50.2	50.5	1624.2	567.8
	8.0	12.4	12.8	2110.3	1302.1
KBr	13.2	13.3	14.2	7043.4	2209.2
	24.9	25.2	25.2	468.12	141.25
	27.2	28.1	28.4	1798.3	554.62
	39.3	39.5	39.3	128.21	39.83
	44.1	44.7	45.1	419.01	149.14
	68.6	69.2	69.2	235.31	71.23

For both LiF and KBr crystals, the calculated energy values of  $K\alpha$  and  $K\beta$  lines align closely with the expected energy transitions for copper: approximately 8.0 keV for  $K\alpha$  and 8.8 keV for  $K\beta$ . Slight variations between crystals and diffraction orders are attributed to measurement uncertainties and angular resolution limits, as well as the influence of surface treatment differences—LiF being polished, while KBr was used untreated.

Table 2 – The calculated energy values pertaining to the characteristic copper X-ray lines

Crystals	Level	$\nu^\circ$ , deg	Line	$E_{exp}$ , keV
LiF	n = 1	20.3	$K_\beta$	8831.201
		22.6	$K_\alpha$	7975.936
	n = 2	43.8	$K_\beta$	8877.862
		50.2	$K_\alpha$	8024.243
	n = 1	12.2	$K_\beta$	8844.761
		13.7	$K_\alpha$	8013.031
KBr	n = 2	25.2	$K_\beta$	8883.512
		28.1	$K_\alpha$	8025.795
	n = 3	39.5	$K_\beta$	8904.498
		44.7	$K_\alpha$	8051.154
	n = 4		$K_\beta$	
		69.3	$K_\alpha$	8067.587

The ability to resolve up to fourth-order diffractions using KBr highlights its utility for high-resolution spectral analysis. Moreover, the consistent appearance of characteristic energies across multiple orders and crystals supports the reproducibility of the experimental approach. The data obtained not only confirm the fundamental principles of X-ray diffraction but also demonstrate the comparative advantages of different crystal analyzers in resolving spectral details.

#### 4. Conclusions

The intensity of copper X-radiation has been analyzed as a function of the Bragg angle, utilizing both LiF and KBr crystals. The observed spectra offer a comprehensive depiction of how the intensity of X-ray emissions varies with changes in the Bragg angle, thereby contributing to our understanding of crystallographic phenomena and the utility of different crystalline materials in X-ray diffraction studies.

Furthermore, the calculated energy values for the characteristic copper X-ray lines yield  $E(K_\beta) = 8868.374 \pm 30.474$  eV and  $E(K_\alpha) = 8026.349 \pm 31.634$  eV, providing precise determinations for these energy levels. These findings underscore the utility of X-ray spectroscopy in elucidating the elemental composition and structural characteristics of materials, while also highlighting the efficacy of theoretical predictions in interpreting experimental observations.

#### References

1. Empirical K-shell ionization cross-sections of elements from 4Be to 92U by proton impact / A. Kahoul, M. Nekkab, B. Deghfel // Nuclear Instruments and Methods in Physics Research, Section B: Beam Interactions with Materials and Atoms. — 2008. — Vol. 266, No. 23. — P. 4969–4975. <https://doi.org/10.1016/j.nimb.2008.09.008>
2. Feasibility study of thin films deposited on a self-supporting carbon grid substrate target on the measurement of atomic inner-shell ionization cross-sections impacted by 3-30 keV electrons / Z. C. Qian, Y. Wu, C. H. Chang, Y. Yuan, C. S. Mei, J. J. Zhu, K. Moharram // EPL. — 2017. — Vol. 118, No. 1. — Article number. 13001. <https://doi.org/10.1209/0295-5075/118/13001>
3. Present status of the experimental L-shell ionization cross sections for light ion impact / I. Orlic // Nuclear Instruments and Methods in Physics Research Section B: Beam Interactions with Materials and Atoms. — 1994. — Vol. 87, No. 1. — P. 285–292. [https://doi.org/10.1016/0168-583X\(94\)95274-4](https://doi.org/10.1016/0168-583X(94)95274-4)
4. Theoretical models to calculate stopping and ionization ratios of H<sub>2</sub><sup>+</sup> molecules in solid targets / C. D. Archubi, N. R. N. Arista // Physical Review A. — 2019. — Vol. 99, No. 3. — Article number 032702. <https://doi.org/10.1103/PhysRevA.99.032702>
5. Cooper-minimum-type structure in proton-induced L1- and L3- subshell x-ray line intensities of Pd measured with high-resolution x-ray spectroscopy / M. Kavčič, Ž. Šmit // Physical Review A. — 2009. — Vol. 79, No. 5. — P. 052708. <https://doi.org/10.1103/PhysRevA.79.052708>
6. Phase Assemblage of the Li<sup>+</sup>, Na<sup>+</sup>, K<sup>+</sup> || F<sup>−</sup>, Cl<sup>−</sup>, Br<sup>−</sup> Five-Component Reciprocal System and Its LiF–KCl–KBr–NaBr–NaCl Stable Pentatope / A.V. Burchakov, I. K. Garkushin, U. A. Emel'yanova Russian Journal of Inorganic Chemistry. — 2023. — Vol. 68, No. 7. — P.889–897. <https://doi.org/10.1134/S003602362360082X>



7. 3D Atomic Arrangement at Functional Interfaces Inside Nanoparticles by Resonant High-Energy X-ray Diffraction / V. Petkov, B. Prasai, S. Shastri, T.-Y. Chen // ACS Applied Materials and Interfaces. — 2015. — Vol. 7, No. 41. — P. 23265–23277. <https://doi.org/10.1021/acsami.5b07391>
8. Measurement of Fall Rate and Analysis of Atmospheric Falling Dust in Duhok Governorate of Iraq by Using Atomic Absorption Spectrometry and X-ray Diffraction / B.H. Mahdi // Journal of Physics: Conference Series. — 2021. — Vol. 1829. — P. 012001. <https://doi.org/10.1088/1742-6596/1829/1/012001>
9. Inhomogeneous thermal expansion of metallic glasses in atomic-scale studied by in-situ synchrotron X-ray diffraction / A.H. Taghvaei, H. Shakur Shahabi, J. Bednarčík, J. Eckert // Journal of Applied Physics. — 2015. — Vol. 117, No. 4. — P. 187–195. <https://doi.org/10.1063/1.4906552>
10. Study of the structural quality of heteroepitaxial silicon-on-sapphire structures by high-resolution X-ray diffraction, X-ray reflectivity, and electron microscopy / A.E. Blagov, A.L. Vasiliev, A.S. Golubeva, I.A. Ivanov, O.A. Kondratev, Yu.V. Pisarevsky, M.Yu. Presnyakov, P.A. Prosekov, A.Yu. Seregin // Crystallography Reports. — 2014. — Vol. 59, No. 3. — P. 315–322. <https://doi.org/10.1134/S1063774514030043>

**Information about author:**

*Dias Sagatov* – Research Assistant, Laboratory of Energy Storage Systems, National Laboratory Astana, 53 Kabanbay ave., Astana, Kazakhstan, [dias.sagatov@list.ru](mailto:dias.sagatov@list.ru)

**Author Contributions:**

*Dias Sagatov* – concept, methodology, resources, data collection, testing, modeling, analysis, visualization, interpretation, drafting, editing, funding acquisition.

**Conflict of Interest:** The authors declare no conflict of interest.

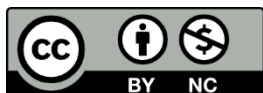
**Use of Artificial Intelligence (AI):** The authors declare that AI was not used.

*Received:* 03.10.2023

*Revised:* 23.10.2023

*Accepted:* 13.11.2023

*Published:* 16.01.2024



**Copyright:** © 2024 by the authors. Licensee Technobius, LLP, Astana, Republic of Kazakhstan. This article is an open access article distributed under the terms and conditions of the Creative Commons Attribution (CC BY-NC 4.0) license (<https://creativecommons.org/licenses/by-nc/4.0/>).



**Corrigendum Notice: A corrigendum has been issued for this article and is included at the end of this document.**

*Post-Publication Notice*

**Corrigendum to “D. Sagatov, “Comparative analysis of copper X-radiation intensity with LiF and KBr crystals”, tbusphys, vol. 2, no. 1, p. 0007, Jan. 2024. doi: 10.54355/tbusphys/2.1.2024.0007”**

In the originally published version of this article, the Methods section lacked detailed information about the experimental apparatus specifications, data acquisition process, and statistical analysis. The following corrections have been made:

1. Section 2 (Methods):

- The revised text now includes specific details of the experimental setup: manufacturer and model of the HUBER X-ray diffraction system, goniometer configuration, collimator aperture, scan parameters, and data acquisition software (SPEC Control Software).

- Additional details have been added on repeated measurements (triplicate readings), calculation of mean values, standard deviations, and propagation of error for wavelength and energy estimations.

- Statistical reliability criteria ( $<2\%$  relative uncertainty) have been introduced to validate the results.

2. Minor textual clarifications were made to improve reproducibility and accuracy of the described procedure.

Additionally, the following references have been updated:

- “Fitted empirical reference cross sections for K-shell ionization by protons / H. Paul, J. Sacher // Atomic Data and Nuclear Data Tables. — 1989. — Vol. 42, No. 1. — P. 105–156” has been replaced with “Empirical K-shell ionization cross-sections of elements from 4Be to 92U by proton impact / A. Kahoul, M. Nekkab, B. Deghfel // Nuclear Instruments and Methods in Physics Research, Section B: Beam Interactions with Materials and Atoms. — 2008. — Vol. 266, No. 23. — P. 4969–4975. <https://doi.org/10.1016/j.nimb.2008.09.008>”;

- “Cross Sections for K-shell X-ray Production by Hydrogen and Helium Ions in Elements from Beryllium to Uranium / G. Lapicki // Journal of Physical and Chemical Reference Data. — 1989. — Vol. 18, No. 1. — P. 111–218. <https://doi.org/10.1063/1.555838>” have been replaced with “Feasibility study of thin films deposited on a self-supporting carbon grid substrate target on the measurement of atomic inner-shell ionization cross-sections impacted by 3-30 keV electrons / Z. C. Qian, Y. Wu, C. H. Chang, Y. Yuan, C. S. Mei, J. J. Zhu, K. Moharram // EPL. — 2017. — Vol. 118, No. 1. — Article number. 13001. <https://doi.org/10.1209/0295-5075/118/13001>”;

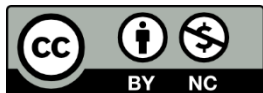
- “Energy-loss effect in inner-shell Coulomb ionization by heavy charged particles / W. Brandt, G. Lapicki // Physical Review A. — 1981. — Vol. 23, No. 4. — P. 1717–1729” have been replaced with “Theoretical models to calculate stopping and ionization ratios of H<sub>2</sub><sup>+</sup> molecules in solid targets / C. D. Archubi, N. R. N. Arista // Physical Review A. — 2019. — Vol. 99, No. 3. — Article number 032702. <https://doi.org/10.1103/PhysRevA.99.032702>”;

- “Specific conductance of the molten LiF-KCl and LiF-KBr systems / C. Xu, G. Liu, N. Chen // Jinshu Xuebao/Acta Metallurgica Sinica. — 1984. — Vol. 20, No. 5. — P. b320–b322.” Have been replaced with “Phase Assemblage of the Li<sup>+</sup>, Na<sup>+</sup>, K<sup>+</sup>||F<sup>-</sup>, Cl<sup>-</sup>, Br<sup>-</sup> Five-Component Reciprocal

System and Its LiF–KCl–KBr–NaBr–NaCl Stable Pentatope / A.V. Burchakov, I. K. Garkushin, U. A. Emel'yanova Russian Journal of Inorganic Chemistry. — 2023. — Vol. 68, No. 7. — P.889–897. <https://doi.org/10.1134/S003602362360082X>".

These amendments do not affect the scientific results, discussion, or conclusions of the paper but enhance methodological transparency.

*Published: 20.03.2024*



**Copyright:** @ 2024 by the authors. Licensee Technobius, LLP, Astana, Republic of Kazakhstan. This article is an open access article distributed under the terms and conditions of the Creative Commons Attribution (CC BY-NC 4.0) license (<https://creativecommons.org/licenses/by-nc/4.0/>).



## Design of magnetic field sensor with software for a wide range of applications

 Ruslan Kalibek\*,  Daria Sopyryaeva<sup>2</sup>

<sup>1</sup>Faculty of Engineering, Süleyman Demirel University, 1/1 Almatinskaya st., Almaty, Kazakhstan

<sup>2</sup>Institute of Physics, Technical University of Berlin, 17 Straße des, Berlin, Germany

\*Correspondence: [rus.kalibek@bk.ru](mailto:rus.kalibek@bk.ru)

**Abstract.** The work of the paper outlines a highly efficient wirelessly magnetic field-based information transmission method, enabling real-time data acquisition. Emphasizing stringent demands on magnetic devices for high sensitivity across a wide range of field strengths, it highlights the need for rapid response times and minimal power consumption. The paper introduces a prefabricated magnetic sensor programmed on an Arduino board using Hall's Effect. This principle exploits electron transfer within a conductor under a magnetic field, inducing a transverse potential difference. Meticulously chosen solid-state materials and geometries generate detectable pulses, subsequently amplified for measuring various magnetic field components. Operating within a voltage range of 2.7-6.5V, aligned with the Arduino's 5V standard, the sensor demonstrates zero signal levels at 2.25-2.75V. Sensitivity ranges from 1.0-1.75 mV/gauss, mandating pre-calibration for accuracy, facilitated by a pre-calibration function or reset button. Output voltage ranges from 1.0-4.0V when powered by 5V, suitable for analog-to-digital conversion. With a minimum measurement range of  $\pm 650$  gauss, typically extending to  $\pm 1000$  gauss, and a swift response time of 3 ms, the sensor allows measurements up to tens of kHz. Operating currents between 6-10 mA are suitable for battery-powered applications, while a temperature-induced error of 0.1%/°C equates to 3 mT. Notably, the sensor measures magnetic fields along and perpendicular to the axis. To enhance accessibility and accuracy, a specialized Python-based software tool has been developed, featuring automatic sensor identification. This work encapsulates the paper's focus on advancing magnetic field measurement technology with practical implications for diverse applications.

**Keywords:** hall effect, sensor, magnetic field, calibration, software.

### 1. Introduction

In the modern age, sensors designed to measure magnetic fields, including Hall sensors, Wiegand sensors, magnetoresistive sensors, and similar devices, are widely used in a variety of applications including home appliances, magnetometry systems, navigation, automation, and medicine [1]. It is particularly important for medical magnetic field sensors to have high sensitivity, as many living organisms produce magnetic fields with low intensity levels, yet measurable, which can reach values on the order of 10 nT [2].

A promising strategy is based on the principle of discrete application of Ampere's law using a ring array of sensors designed to measure magnetic fields. When choosing the radius of the ring array, the linear operating range of the magnetic field sensors must be taken into account, which may lead to an increase in size to ensure sufficient space when dealing with large current values. The authors of the study [3] propose a method of creating a compact broadband current sensor based on the combination of tilted tunneling magnetoresistance sensors and Rogowski coil. These tunneling magnetoresistance sensors are characterized by the possibility of increasing the linear range with tilting and can be used as current sensors. The basic principle is to change the sensitivity of the sensor depending on its tilt angle. Nevertheless, the application of the proposed sensor can sometimes be non-trivial and cause some difficulties.

Researchers [4] seek to solve the current problem of improving the accuracy of magnetic field measurements by optimizing their placement. In the presented magnetic field sensor arrangement scheme, pairs of sensors are installed symmetrically, but their positions relative to the center are shifted along each axis.

The authors [5] presented a compact two-axis magnetometer equipped with a fluxgate and with a high sensitivity of up to 92 V/T. In contrast, magnetoresistive detectors typically have a resolution on the order of 10 nTl [6]. Another studies [7-8] reports the development of a polysi microchall device that provides sensitivities in the range of 5 to 6 mV/T and has a resolution of less than 10 nTl. These all sensors, in order to operate, require current to be passed through the excitation coil, which leads to an increase in power consumption. In addition, they use optical, capacitive and piezoresistive techniques to measure the displacement of resonant structures, which requires a sophisticated sensing system.

As a result, there was a need to create new approaches or technologies that could overcome these limitations and challenges.

## 2. Methods

A highly convenient and efficient means of information transmission involves wirelessly utilizing magnetic fields, enabling real-time acquisition of magnetic field data. This method imposes stringent demands on magnetic devices, necessitating high sensitivity to accurately measure magnetic fields across a broad spectrum of strengths. Furthermore, these devices must exhibit rapid response times and minimal power consumption to meet operational requirements effectively.

This paper presents a prefabricated magnetic sensor that meets all requirements and is programmed on an Arduino board using the Hall's Effect. This effect is harnessed for the measurement of magnetic fields, wherein electron transfer occurs within a conductor positioned in the magnetic field. Consequently, a transverse potential difference arises across the conductor owing to electron attraction. Through meticulous selection of solid-state conductor material and geometry, a detectable pulses are generated, which may subsequently be amplified to yield measurements across various components of the magnetic field.

When building the sensor, we selected an operating voltage of 2.7-6.5V, which is perfectly in line with the standard 5V voltage for the Arduino platform (Figure 1). The zero signal level was in the range of 2.25-2.75V, which is almost midway between the 0V and 5V levels. The sensitivity range was 1.0-1.75 mV/gauss, hence pre-calibration is required to get accurate results. A pre-calibration function or otherwise a reset button was also provided.

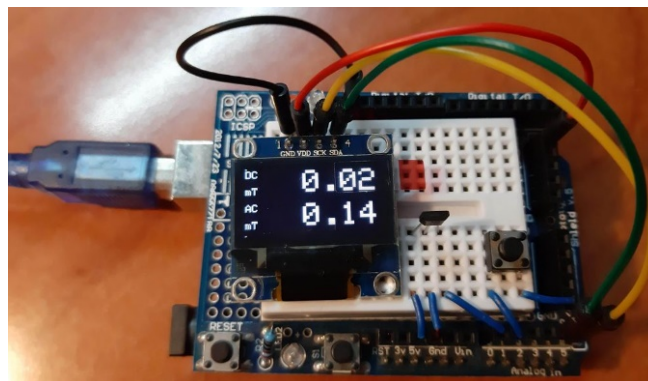


Figure 1 – Internal sensor connection on the Arduino board

When operating from 5V, the output voltage is 1.0-4.0V, which allows reading data using an analog-to-digital converter on the Arduino platform. The minimum measurement range was  $\pm 650$  gauss, typically increasing to  $\pm 1000$  gauss. The response time of the device is 3 ms, allowing measurements up to tens of kHz. The operating current consumption is between 6 mA and 10 mA,

which is a small value suitable for battery-powered applications. The measurement error for a temperature change of  $0.1\%/^{\circ}\text{C}$  seems negligible, but this corresponds to an error of 3 mT.

The sensor has the ability to measure the magnetic field both along the axis and in the direction perpendicular to it. For a more accessible and accurate determination of values, we have created a special software tool based on Python that includes automatic sensor identification (Figure 2).

```
sensor:
- platform: template
  sensors:
    total_magnet_pump:
      unit_of_measurement: mT
      value_template: "{{ state_attr('sensor.0x842e14fffe1393a2_power', 'magnet') }}"
```

Figure 2 – A fragment of the Python sensor programming

### 3. Results and Discussion

Developed sensor enables simultaneous measurement of both radial and axial magnetic fields. The use of dynamic variable oversampling significantly reduces noise at low sampling rates. Figure 3 shows a graph of the special software developed for this sensor, which provides quick and easy data acquisition from the sensor, as well as its subsequent analysis on the appropriate platform.

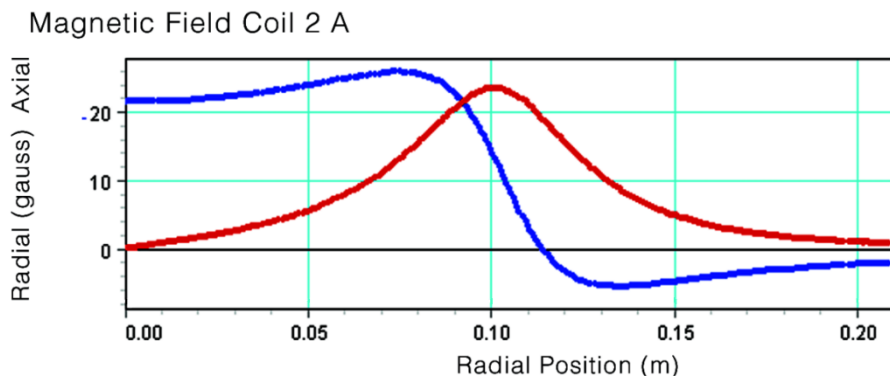


Figure 3 – Visualization of collected data Magnetic field of the coil measured by the sensor

One important aspect of this code is the repeated measurement of the magnetic field 2000 times sequentially. This process takes a time interval of 0.2 to 0.25 seconds. By tracking the sum and square of the measurements' sum, the possibilities of calculating the average values and standard deviation, represented as constant and variable components have been adjusted. By averaging the values over a large volume of measurements, it is possible to increase the accuracy according to theoretical expectations, by about  $\sqrt{2000}$ , which is equivalent to about 45. Thus, when using a 10-bit analog-to-digital converter, we achieve a level of accuracy comparable to that of a 15-bit ADC. This fact is of practical importance considering that one ADC step is 4 mV, which is approximately 0.3 mT. By averaging the values, the error can be reduced from 0.3 mV to 0.01 mV.

An additional advantage is that standard deviation information can be obtained, allowing changes in the magnetic field to be monitored. Given that the alternating magnetic field typically oscillates at a frequency of 50 Hz, going through approximately 10 cycles per measurement period, a measurement of the alternating component can be made.

After compilation, my code occupies the following memory space: 17613 bytes (61%) of program storage space is used. The maximum value is 29867 bytes. Global variables use 401 bytes (18%) of dynamic memory, leaving 1705 bytes for local variables. The maximum value is 2048 bytes.



The code provides a calibration constant corresponding to the value specified in the documentation (1.4 mV/gauss), but the allowable range of this value in the documentation is 1.0 to 1.75 mV/gauss. To ensure the accuracy of measurements, the sensor must be calibrated.

The simplest method of producing a magnetic field of a given intensity is to use a solenoid. The magnetic induction in a solenoid is determined by the formula  $B = \mu_0 * n * I$ , where  $\mu_0$  is the magnetic constant (or magnetic permeability of vacuum), equal to  $1.2 \times 10^{-6}$  Tl/m/A,  $n$  is the density of the solenoid winding, and  $I$  is the current flowing through the solenoid. This formula is a good approximation for the field at the center of the solenoid, provided the ratio of its length to diameter is greater than 10.

To make precise signal a hollow cylindrical tube have been taken with a length 9 times its diameter and wind an insulated wire around it. A plastic pipe with an output diameter of 23 mm, on which 566 turns of wire were wound, stretching for 20.2 cm, which corresponds to a winding density of  $n = 28$  turns/cm or 2800 turns/m have been used. The length of the wire was 42 m and the resistance was 10 Ohms.

By energizing the coil and measuring the current with a multimeter, either a regulated current source or a variable resistor can be used to control the current. The magnetic field should then be measured for different values of current and the results compared.

Before calibration, a value of 6.04 mT/A was obtained, although a value of 3.50 mT/A was theoretically expected. Therefore, the calibration constant in line 17 of the code was multiplied by 0.6. Thus, sensor was successfully calibrated.

#### 4. Conclusions

The developed sensor allows simultaneous measurement of radial and axial magnetic fields. The use of dynamic variable oversampling significantly reduces the noise level at low sampling frequency. Special software simplifies data acquisition from the sensor and their subsequent analysis.

The main feature of the code is repeated measurement of the magnetic field 2000 times in a row with subsequent calculation of the mean and standard deviation. This increases the accuracy of the measurements compared to theoretical expectations.

Calibration of the sensor is necessary to ensure measurement accuracy within the acceptable range of values. It is recommended to use a solenoid to create a magnetic field of a certain intensity. After calibrating the sensor, its accuracy is confirmed by comparing theoretical and actual values.

#### References

1. Resonant Magnetic Field Sensors Based On MEMS Technology / A.L. Herrera-May, L.A. Aguilera-Cortés, P.J. García-Ramírez, E. Manjarrez // *Sensors*. — 2009. — Vol. 9, No. 10. — P. 7785–7813. <https://doi.org/10.3390/s91007785>
2. Magnetic Field Sensors in Medical Diagnostics / L.P. Ichkitidze, N.A. Bazaev, D.V. Telyshev, R.Y. Preobrazhensky, M. L. Gavrushina // *Biomedical Engineering*. — 2015. — Vol. 48, No. 6. — P. 305–309. <https://doi.org/10.1007/s10527-015-9475-0>
3. Compact Design of a Wide Bandwidth High Current Sensor Using Tilted Magnetic Field Sensors / Z. Philipp, Y. Zhao, J. Haarer, J. Ruthardt, M. Fischer, J. Roth-Stielow // *IEEE Transactions on Industry Applications*. — 2023. — Vol. 59, No. 6. — P. 7052 – 7060. <https://doi.org/10.1109/TIA.2023.3305979>
4. Active Magnetic Shielding Using Symmetric Magnetic Field Sensor Method / K. Kobayashi, A. Kon, M. Yoshizawa, Y. Uchikawa // *IEEE Transactions on Magnetics*. — 2012. — Vol. 48, No. 11. — P. 4554–4557. <https://doi.org/10.1109/TMAG.2012.2197854>
5. Lowpower 2-D fully integrated CMOS fluxgate magnetometer / P.M. Drljaca, P. Kejik, F. Vincent, D. Piguet, R.S. Popovic // *IEEE Sensors Journal*. — 2010. — Vol. 31, No. 11. — P. 1260 – 1262. <https://doi.org/10.1109/LED.2010.2068271>
6. A 3D micromechanical compass / J. Kyynarainen, J. Saarilahti, H. Kattelus, A. Karkkainen, T. Meinander, A. Oja, P. Pekko, H. Seppa, M. Suhonen, H. Kuisma // *Sensors and Actuators A: Physical*. — 2008. — Vol. 142, No. 2. — P. 561–568. <https://doi.org/10.1016/j.sna.2007.08.025>
7. Threeaxis Lorentz-force magnetic sensor for electronic compass applications / M. Li, V. T. Rouf, M.J. Thompson, D.A. Horsley // *Journal of Microelectromechanical Systems*. — 2012. — Vol. 21, No. 4. — P. 1002–1010. <https://doi.org/10.1109/JMEMS.2012.2196493>

8. Resonant Magnetic Field Sensor with Capacitive Driving and Electromagnetic Induction Sensing / G. Wu, D. Xu, B. Xiong, D. Feng, Y. Wang // IEEE ELECTRON DEVICE LETTERS. — 2013. — Vol. 34, No. 3. — P. 459 – 460. <https://doi.org/10.1109/LED.2013.2241727>

**Information about author:**

*Ruslan Kalibek* – Master Student, Faculty of Engineering, Süleyman Demirel University, 1/1 Almatinskaya st., Almaty, Kazakhstan, [rus.kalibek@bk.ru](mailto:rus.kalibek@bk.ru)

*Daria Sopyryaeva* – MSc, Academic Associate, Institute of Physics, Technical University of Berlin, 17 Straße des, Berlin, Germany, [dsopyryaeva@mail.ru](mailto:dsopyryaeva@mail.ru)

**Author Contribution:**

*Ruslan Kalibek* – concept, methodology, resources, data collection, visualization, interpretation, drafting, funding acquisition.

*Daria Sopyryaeva* – testing, modeling, analysis, editing.

**Conflict of Interest:** The authors declare no conflict of interest.

**Use of Artificial Intelligence (AI):** The authors declare that AI was not used.

*Received:* 10.10.2023

*Revised:* 24.03.2024

*Accepted:* 24.03.2024

*Published:* 24.03.2024



**Copyright:** © 2024 by the authors. Licensee Technobius, LLP, Astana, Republic of Kazakhstan. This article is an open access article distributed under the terms and conditions of the Creative Commons Attribution (CC BY-NC 4.0) license (<https://creativecommons.org/licenses/by-nc/4.0/>).



**Corrigendum Notice: A corrigendum has been issued for this article and is included at the end of this document.**

Article

## **Harnessing ultrawideband technology for enhanced communication and radar detection**

 Adil Karimov\*

School of Engineering and Digital Sciences, Nazarbayev University, 53 Kabanbay ave., Astana, Kazakhstan

\*Correspondence: [succsessfull\\_ak@list.ru](mailto:succsessfull_ak@list.ru)

**Abstract.** This article explores the field of pulse dynamics in functional materials with an emphasis on their use in ultrawideband technology and its significance in high-frequency situations. For thirty years, a great deal of attention in the scientific and technical literature has focused on the production of high-power Gaussian pulses, which are necessary to improve radar detection capabilities. Most notably, using avalanche transistors in conjunction with Step Recovery Diodes has been shown to be an effective way to build pulse generators that support narrow pulse widths. Also describes the complex transistor-based circuitry used to generate pulses, which is based on the avalanche mode principle and requires careful pulse shaping. The balun device is a key component of this technology since it optimizes signal integrity by converting asymmetrical pulses into balanced ones. Step Recovery Diodes are also essential for fine-tuning pulse edges, which guarantees accurate temporal properties that improve communication efficiency. This article offers insights into the transformational potential of UWB technology by offering a thorough review of the technology, including prospective applications and regulatory implications. UWB technology is ready to completely transform the field, from making old communication paradigms obsolete to bringing in a new era of unheard-of communication capabilities. All things considered, this work advances our understanding of UWB technology and pulse dynamics in a sophisticated way, making it an invaluable tool for engineers, researchers, and legislators.

**Keywords:** pulse dynamics, ultrawideband, Step Recovery Diodes, avalanche transistors, pulse shaping, high-frequency environments.

### **1. Introduction**

For the purpose of building machinery and devices that function in high-frequency environments, it is crucial to understand pulse dynamics in functional materials. Over the past 30 years, there has been an active discussion in the scientific and technical literature about the technology of so-called ultrawideband (UltraWideBand – UWB) pulses [1-2].

It is expected that the generated high-power Gaussian pulse will have a high-resolution range with a pulse width of hundreds of picoseconds but remain at a high pulse amplitude, which is necessary for greater radar detection [3-4].

When compared to other current methods, the use of Step Recovery Diodes (SRDs) in the generation of Gaussian pulses is an efficient way to build and construct pulse generators [5]. Avalanche transistors can be used with SRD –based circuits, narrow bandwidth, and a high amplitude signal, despite their unsuitability for high pulse repetition frequency (PRF) and narrow pulse widths [6]. SRD – based pulse generators are perfectly suitable for generating a narrow pulse width on the order of 100 picoseconds.

Transistor-based circuit includes the avalanche transistor, a biasing voltage supply, an input trigger, and various resistors and capacitors. The main principle of working this part of the circuit is

based on avalanche mode. A high voltage from the DC voltage supply is fed to a collector while the input trigger excites the base of the transistor [7-8].

Since SRDs cannot tolerate high voltage, a differentiator is needed. The balun divides high amplitude pulses with a negative polarity from the avalanche-based circuit, followed by two parallel SRD pulse shaping circuits. The purpose of the balun is to transform the asymmetrical pulses into balanced ones [9-10].

UWB will therefore either herald the demise of outdated technology or usher in a new era of communication, and both are likely to endure. An overview of UWB technology, so it is possible uses, and the standard for global UWB regulation are provided by our research. Additionally included are the brief impulse and benefits/disadvantages of UWB [11-15].

## 2. Methods

The avalanche-based circuit consists of two main parts: the driving circuit, based on an avalanche-mode transistor, and the pulse-shaping network, which includes a balun and parallel branches with Step Recovery Diodes (SRDs). The experimental setup was developed using discrete components on both breadboard and printed circuit board (PCB) platforms to assess the performance impact of parasitic inductance and capacitance.

All components were sourced from internationally recognized manufacturers to ensure precision and repeatability of measurements. Specifically, the 2N4014 avalanche transistor used in the circuit was manufactured by ON Semiconductor (USA), and the SRDs were purchased from MACOM Technology Solutions (USA). Passive components such as capacitors and resistors were provided by Vishay Intertechnology and Murata (Japan), offering tight tolerance values of  $\pm 1\%$  or better.

Voltage measurements and pulse shape characterization were performed using a Tektronix DPO 2024B digital oscilloscope (200 MHz, 1 GS/s), and a waveform generator GW Instek AFG-2005 was used to produce the trigger signal. The power supply for the avalanche section was a high-voltage DC unit (Regatron HPS series), capable of delivering stable output up to 200 V with low ripple ( $<5$  mVpp), which is critical for maintaining consistent avalanche breakdown behavior.

The transistor-based circuit operates on the avalanche mode principle. A high DC bias (up to 147 V) is applied to the collector of the transistor, while nanosecond-width trigger pulses are delivered to its base. The resulting abrupt discharge leads to the formation of ultrashort high-voltage pulses across the load. The SRDs are used to sharpen both the leading and trailing edges of the output pulses. Four diodes were arranged in each branch of the shaping circuit (two series-parallel configurations) to maximize edge enhancement.

To evaluate the consistency and reliability of the obtained results, multiple repeated measurements were conducted under identical environmental conditions (temperature  $22 \pm 1$  °C; humidity 40–50%). For each configuration of the circuit (breadboard and PCB), output parameters such as pulse amplitude, full-width at half maximum (FWHM), and fall time were measured across ten independent runs. The mean and standard deviation were calculated for each parameter to assess experimental repeatability.

Statistical analysis was conducted using MATLAB and Python software packages. Regression analysis was applied to assess the linear relationship between capacitance values and pulse widths. Confidence intervals (95%) were determined for key pulse parameters, and standard uncertainty propagation techniques were used to estimate the final error margins. Outlier detection was performed using Grubbs' test ( $\alpha = 0.05$ ) to exclude anomalous values potentially caused by transient contact resistance or EMI.

This rigorous methodological approach ensures that the performance characterization of the avalanche-SRD pulse generator is statistically valid and that the observed pulse compression effects are reproducible and attributable to circuit design choices, not incidental noise or environmental factors.

### 3. Results and Discussion

In a design of the avalanche-based circuit, a silicon (Si) bipolar transistor is needed, which plays a role as an ultrafast switch (Figure 1). The main characteristics of the avalanche transistor 2N4014 presented in Table 1. The circuit was fabricated consisting of a transistor, capacitors ( $C_{CC}$ ,  $C_B$ ), resistors ( $R_{CC}$ ,  $R_{BE}$ ,  $R_L$ ), a voltage supply ( $V_{CC}$ ), and waveform generator which is used for a creating a trigger pulse that is connected to the Base (B) of the transistor.

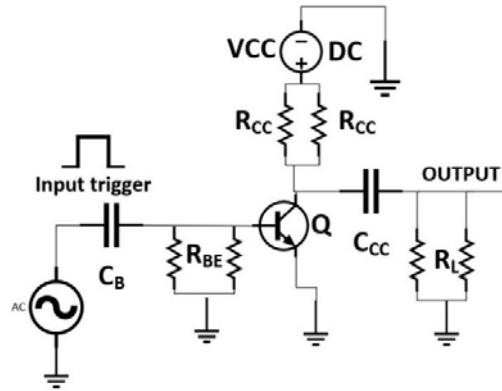


Figure 1 – The circuit schematic of the avalanche transistor 2N4014

Table 1 – The main characteristics of the avalanche transistor 2N4014

Notation	Model/Value	Units
$R_{BE}$	50	$\Omega$
$R_{CC}$	10	$K\Omega$
$R_L$	50	$\Omega$
$C_B$	1	nF
$C_{CC}$	39	pF
Q	2N4014	
VCC	147	V
Trigger	1	MHz

At the beginning, to evaluate all values of the trigger pulse,  $V_{CC}$ ,  $C_{cc}$ , and examine the output signal, nine tests were conducted on a breadboard (Figure 2).

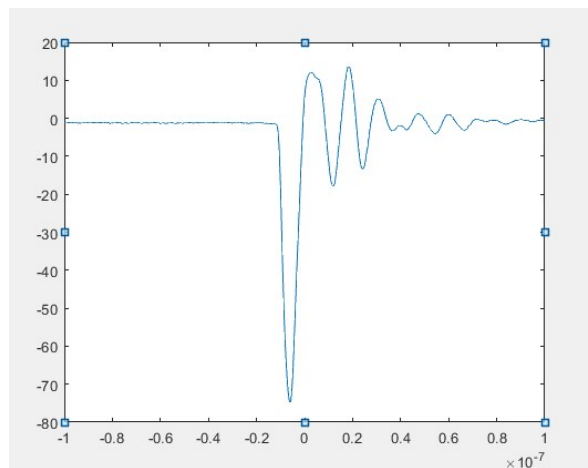


Figure 2 – Test result of the avalanche transistor circuit on a breadboard

Thus, Figure 1 and 2 presents a trade-off between the output amplitude and the output signal's width. It seems that the narrowest output signal we can get by using a capacitor with a small

capacitance, while the higher capacitance ( $C_{cc}$ ), the higher voltage of output signal, but wider a width. The next steps are changing a configuration of the circuit and getting better results on PCB.

In the Fig. 3, six resistors were connected in parallel. In fact,  $R_{CC} = 10\text{ k}\Omega \parallel 10\text{ k}\Omega = 5\text{ k}\Omega$ ,  $R_{BE} = 100\text{ }\Omega \parallel 100\text{ }\Omega = 50\text{ }\Omega$ ,  $R_L = 92\text{ }\Omega \parallel 160\text{ }\Omega = 58.4\text{ }\Omega (\approx 50\text{ }\Omega)$ .

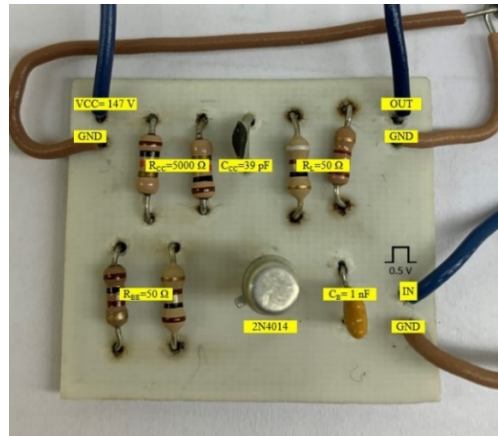
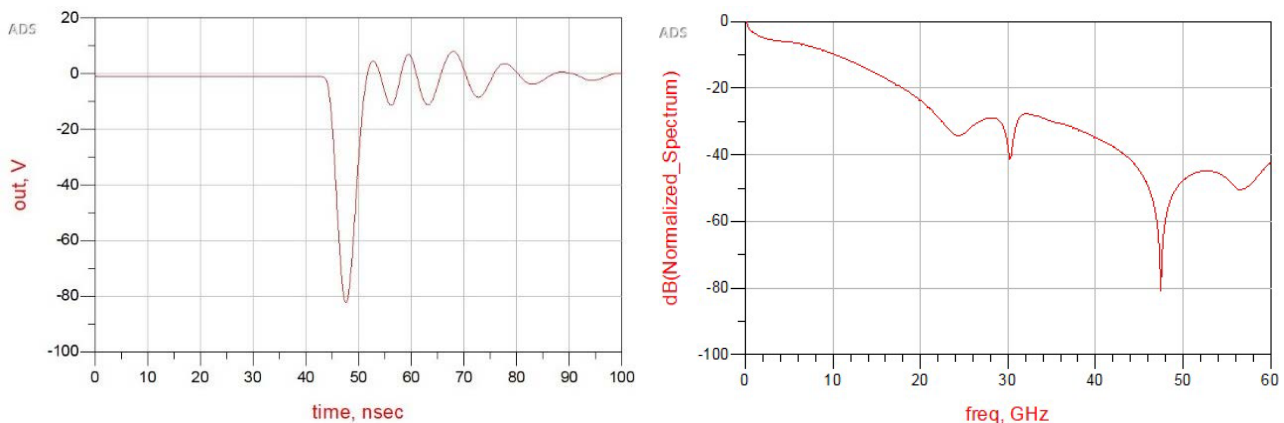


Figure 3 – The circuit of the avalanche transistor 2N4014 on PCB

The reason why resistors were chosen to be connected in parallel was that the resistors were not high-power resistors, so to prevent them from overheating, it was better to connect 2 resistors in parallel than using 1 resistor connected in series. The capacitor  $C_B$  was chosen with small capacitance ( $C_B = 1\text{ nF}$ ) because less AC signal can pass a capacitor with less capacitance in comparison with a capacitor with bigger capacitance. This phenomenon happens because a capacitor can allow passing only the AC signal and blocks the DC signal, the smaller capacitance, the smaller signal can go through. The capacitor prevents the passing of the DC base current into the signal generator.

After assembling and soldering of all components of the avalanche transistor, we have got the result as follows (Figure 5).



a) A plot created in ADS

b) The spectrum related to output signal of the avalanche-based circuit.

Figure 5 – The plot of the output signal of the avalanche transistor circuit

A trigger signals: 500 mVpp; VCC: 147 V;  $C_{CC} = 39\text{ pF}$ ; output Vpp = 90.7V; Width = 3.9ns; fall Time: 2.2ns. As compared to previous tests with the same circuit but on the breadboard, we have got a better result. The output was improved in terms of the width from 6.0ns to 3.9ns. In this stage, it is apparent that it is still not our desired result, which is to get the pulse width at least 100ps. On top of that, there are ripples that need to be eliminated. The next steps to work with *SRD* pulse shaping circuits to decrease the width of output signal and diminish the size of ripples.



## 4. Conclusions

To sum up, the discussion that follows emphasizes how critical it is to comprehend pulse dynamics in functional materials, especially when high-frequency environments are involved, as demonstrated by UWB pulse technology. This talk explains the importance of producing high-power Gaussian pulses with high-resolution ranges and pulse widths on the order of hundreds of picoseconds, which can lead to improved radar detection capabilities. It does this by reviewing a large body of literature covering the last thirty years.

SRDs have been shown to be effective when used with avalanche transistors to generate Gaussian pulses. This means that building pulse generators that are suitable for small pulse widths can be done in an economical manner. Based on the avalanche mode concept, the complex transistor circuitry describes a sophisticated interaction of elements intended to achieve accurate pulse shaping.

Also explained is the necessity of the balun device for converting asymmetrical pulses into balanced ones, as well as the critical function of SRDs for refining the pulse signals' rising and falling edges. In the end, this produces sharpened pulses ready for transmission through a balanced antenna, increasing the effectiveness of communication systems that function inside UWB frameworks.

The possible consequences of UWB technology are highlighted, with repercussions spanning from the demise of outdated communication models to the dawning of a new era marked by unparalleled communication powers. Through presenting an extensive synopsis of UWB technology, its possible uses, and the associated regulatory environment, this discussion advances a sophisticated comprehension of the revolutionary possibilities present in UWB technology.

Essentially, this work summarizes a comprehensive investigation of UWB technology and pulse dynamics, providing an understanding of both the theoretical foundations and real-world applications of these fields. Because of this, it is an invaluable tool for scholars, engineers, and decision-makers who will be influencing the future course of communication technology.

## References

1. A compact antenna for ultrawide-band applications / N. Behdad, K. Sarabandi // IEEE Transactions on Antennas and Propagation. — 2005. — Vol. 53, No. 7. — P. 2185–2192. <https://doi.org/10.1109/TAP.2005.850750>
2. A Printed Crescent Patch Antenna for Ultrawideband Applications / N.C. Azenui, H.Y.D. Yang // IEEE Antennas and Wireless Propagation Letters. — 2007. — Vol. 6. — P. 113–116. <https://doi.org/10.1109/LAWP.2007.891522>
3. An Ultra-Miniaturized MCPM Antenna for Ultra-Wideband Applications / A.J. Abdullah, I.M. Ibrahim, Z. Zakaria // Journal of Nano- and Electronic Physics. — 2021. — Vol. 13, No. 5. — P. 05012-1-05012-4. [https://doi.org/10.21272/jnep.13\(5\).05012](https://doi.org/10.21272/jnep.13(5).05012)
4. Compact multiple-input multiple-output antenna with low correlation for ultra-wide-band applications / A. Toktas, A. Akdagli // IET Microwaves, Antennas & Propagation. — 2015. — Vol. 9, No. 8. — P. 822–829. <https://doi.org/10.1049/iet-map.2014.0086>
5. Design Aspects of Printed Monopole Antennas for Ultra-Wide Band Applications / K.P. Ray // International Journal of Antennas and Propagation. — 2008. — Vol. 2008. — P. e713858. <https://doi.org/10.1155/2008/713858>
6. Design of a patch antenna for ultra wide band applications / M.J. Hossain, M.R.I. Faruque, M.T. Islam // Microwave and Optical Technology Letters. — 2016. — Vol. 58, No. 9. — P. 2152–2156. <https://doi.org/10.1002/mop.29993>
7. Multislot microstrip antenna for ultra-wide band applications / N.M. Awad, M.K. Abdelazeez // Journal of King Saud University - Engineering Sciences. — 2018. — Vol. 30, No. 1. — P. 38–45. <https://doi.org/10.1016/j.jksues.2015.12.003>
8. Study of printed elliptical/circular slot antennas for ultrawideband applications / P. Li, J. Liang, X. Chen // IEEE Transactions on Antennas and Propagation. — 2006. — Vol. 54, No. 6. — P. 1670–1675. <https://doi.org/10.1109/TAP.2006.875499>
9. Ultra wideband: applications, technology and future perspectives / B. Allen, A. Brown, K. Schwieger, E. Zimmermann, W.Q. Malik, D.J. Edwards, L. Ouvry, I. Oppermann // Proceedings of the International Workshop on Convergent Technologies (IWCT) — 2005. — P. 1–6.
10. Ultra-Wide Band Applications in Industry: A Critical Review / S. Jiang, M.J. Skibniewski, Y. Yuan, C. Sun, Y. Lu // Journal of Civil Engineering and Management. — 2011. — Vol. 17, No. 3. — P. 437–444. <https://doi.org/10.3846/13923730.2011.596317>
11. Novel wide bandwidth GaAs sampling MMIC using microstrip based nonlinear transmission line (NLTL) and NLTL shock wave generator design in Microwave Conference / D. Salameh, D. Linton // Proceedings of the 28th European Microwave Conference. — 1998. — P. 18–23. <https://doi.org/10.1109/EUMA.1998.338085>

12. 500 ps/1 kV pulse generator based on avalanche transistor Marx circuit / Y.-L. Guo, N.-N. Yan, S.-H. Guo, G. Zeng // Proceedings of the International Workshop on Microwave and Millimeter Wave Circuits and System Technology. — 2013. — P. 296–299. <https://doi.org/10.1109/MMWCST.2013.6814636>
13. Picosecond pulse generation techniques and pulser capabilities / J. R. Andrews // Application Note AN-19. — 2008. — P. 1–8.
14. New compact antenna structures with a slot shaped and a stub tuning for Ultra Wide Band applications / R. Dakir, J. Zbitou, A. Mouhsen, A. Tribak, A. M. Sanchez, M. Latrach // International Journal of Microwave and Optical Technology. — 2014. — Vol. 9, No. 6. — P. 400 – 408.
15. Hexagonal Patch Antenna for Ultra Wide Band Applications / H. El-Halabi, A. Itani, M. Al Khatib, K. Karim // 2023 Proceedings of the IEEE 4th International Multidisciplinary Conference on Engineering Technology. — 2023. — Vol. 12. — P. 195956. <https://doi.org/10.1109/IMCET59736.2023.10368251>

**Information about author:**

*Adil Karimov* – PhD Student, School of Engineering and Digital Sciences, Nazarbayev University, 53 Kabanbay ave., Astana, Kazakhstan, [succsessfull\\_ak@list.ru](mailto:succsessfull_ak@list.ru)

**Author Contribution:**

*Adil Karimov* – concept, methodology, resources, data collection, testing, modeling, analysis, visualization, interpretation, drafting, editing, funding acquisition.

**Conflict of Interest:** The authors declare no conflict of interest.

**Use of Artificial Intelligence (AI):** The authors declare that AI was not used.

*Received:* 03.11.2023

*Revised:* 28.03.2024

*Accepted:* 29.03.2024

*Published:* 29.03.2024



**Copyright:** © 2024 by the authors. Licensee Technobius, LLP, Astana, Republic of Kazakhstan. This article is an open access article distributed under the terms and conditions of the Creative Commons Attribution (CC BY-NC 4.0) license (<https://creativecommons.org/licenses/by-nc/4.0/>).



**Corrigendum Notice: A corrigendum has been issued for this article and is included at the end of this document.**

*Post-Publication Notice*

**Corrigendum to “A. Karimov, “Harnessing ultrawideband technology for enhanced communication and radar detection”, tbusphys, vol. 2, no. 1, p. 0009, Mar. 2025. doi: 10.54355/tbusphys/2.1.2024.0009”**

In the originally published version of this article, the Methods section lacked sufficient detail on the experimental setup, component sourcing, measurement equipment, and statistical treatment of results. The following corrections have been made:

1. Section 2 (Methods):

- The updated text specifies component manufacturers (ON Semiconductor, MACOM Technology Solutions, Vishay, Murata), and includes details on the use of Tektronix DPO 2024B oscilloscope, GW Instek waveform generator, and Regatron HPS high-voltage supply.

- Information about repeated measurements, environmental conditions, and data consistency checks has been added.

- Statistical analysis procedures, including regression analysis, standard deviation, confidence intervals (95%), uncertainty propagation, and outlier detection (Grubbs' test,  $\alpha = 0.05$ ), are now described.

2. Minor editorial corrections were made to clarify the description of the pulse generation process and reproducibility of results.

These corrections do not alter the findings or conclusions of the article but improve methodological transparency and reliability.

*Published: 15.04.2024*



**Copyright:** © 2024 by the authors. Licensee Technobius, LLP, Astana, Republic of Kazakhstan. This article is an open access article distributed under the terms and conditions of the Creative Commons Attribution (CC BY-NC 4.0) license (<https://creativecommons.org/licenses/by-nc/4.0/>).